

Article

Thermoelectric Properties of Scandium Sesquitelluride

Dean Cheikh ¹, Kathleen Lee ¹, Wanyue Peng ², Alexandra Zevalkink ² , Jean-Pierre Fleurial ¹ and Sabah K. Bux ^{1,*}

¹ Thermal Energy Conversion Research and Advancement Group, Jet Propulsion Laboratory/California Institute of Technology, 4800 Oak Grove Drive, Pasadena, CA 91109, USA; dean.a.cheikh@jpl.nasa.gov (D.C.); Kathy.Lee@jpl.nasa.gov (K.L.); Jean-Pierre.Fleurial@jpl.nasa.gov (J.-P.F.)

² Chemical Engineering and Materials Science Department, Michigan State University, East Lansing, MI 48824, USA; pengwany@msu.edu (W.P.); alexzev@msu.edu (A.Z.)

* Correspondence: Sabah.K.Bux@jpl.nasa.gov; Tel.: +1-818-393-7067

Received: 1 February 2019; Accepted: 27 February 2019; Published: 4 March 2019



Abstract: Rare-earth (RE) tellurides have been studied extensively for use in high-temperature thermoelectric applications. Specifically, lanthanum and praseodymium-based compounds with the Th_3P_4 structure type have demonstrated dimensionless thermoelectric figures of merit (zT) up to 1.7 at 1200 K. Scandium, while not part of the lanthanide series, is considered a RE element due to its chemical similarity. However, little is known about the thermoelectric properties of the tellurides of scandium. Here, we synthesized scandium sesquitelluride (Sc_2Te_3) using a mechanochemical approach and formed sintered compacts through spark plasma sintering (SPS). Temperature-dependent thermoelectric properties were measured from 300–1100 K. Sc_2Te_3 exhibited a peak $zT = 0.3$ over the broad range of 500–750 K due to an appreciable power factor and low-lattice thermal conductivity in the mid-temperature range.

Keywords: thermoelectric; rare-earth telluride; scandium telluride

1. Introduction

Thermoelectric materials are used as solid-state energy conversion devices to transform thermal energy into electrical power. The dimensionless thermoelectric figure of merit is a measure of a material's conversion efficiency and is defined as $zT = \frac{S^2T}{\rho\kappa}$, where S is the Seebeck coefficient, ρ is the electrical resistivity, κ is the thermal conductivity, and T is the absolute temperature. Good thermoelectric materials will have a high Seebeck coefficient, low electrical resistivity, and low thermal conductivity.

One area where thermoelectrics are a key enabling technology is power generation for deep-space exploration vehicles [1–3]. Radioisotope thermoelectric generators (RTGs) utilize thermoelectric materials to convert heat from a decaying radioisotope fuel into electricity to power spacecraft instrumentation. The thermoelectric materials integrated into the RTGs (traditionally Si–Ge alloys, PbTe, or Te–Ag–Ge–Sb) have demonstrated long-term reliability, with the *Voyager 1* and 2 missions continuously operating for over 40 years [2–5]. However, one limitation of these devices is that they exhibit modest thermal-to-electrical system level conversion efficiencies of approximately 6.5% at beginning-of-life, due to the average zT values of the heritage materials being less than 1 over their operating temperature range [1,4]. Hence, identification of materials with high zT values is critical for increasing the efficiencies of RTGs, which would enable greater specific power for future missions.

Rare-earth (RE) tellurides in the range $\text{RE}_{3-x}\text{Te}_4$ ($0 < x < 0.33$) have been studied extensively for potential use in high-temperature thermoelectric applications owing to their excellent thermal

stability and large zT values [6–11]. The favorable thermoelectric properties stem from the complexity of the Th_3P_4 structure type ($\bar{1}43d$) from vacancies on the RE site, which cause low-lattice thermal conductivities (between 0.5 and $1 \frac{\text{W}}{\text{mK}}$ for $\text{La}_{3-x}\text{Te}_4$ and $\text{Pr}_{3-x}\text{Te}_4$) [2,6,7]. The electronic properties of these compounds are also controlled by the RE vacancies. Applying electron counting rules to RE_3Te_4 , each RE cation donates 3 electrons and each Te anion accepts 2 electrons. Therefore, when $x = 0$ (RE_3Te_4) there is one free electron in the structure, and a degenerate semiconducting behavior is observed. When $x = 0.33$ ($\text{RE}_{2.67}\text{Te}_4$ or RE_2Te_3), no excess electrons are present and they are semi-insulating. Additionally, these materials have favorable band structures that allow them to maintain large Seebeck coefficients at high carrier concentrations [12,13]. As a result, several $\text{RE}_{3-x}\text{Te}_4$ compounds have peak zT values over 1, the highest being $\text{Pr}_{3-x}\text{Te}_4$ with a $zT = 1.7$ at 1200 K for $x = 0.23$ [6,7]. Therefore, it is of interest to investigate other rare-earth tellurides to attain higher figures of merit.

Though not a member of the lanthanide series, scandium is chemically similar to the RE elements [14]. The primary use of scandium is in aluminum alloys for aerospace components, where adding small amounts of scandium significantly improves the specific strength and increases the recrystallization temperatures [15–18]. Scandium additions to SrCoO_3 -based solid oxide fuel cells have also been shown to significantly increase their oxygen conductivity and improve the overall performance [19–21]. Despite the benefits to several applications, the study of scandium-containing compounds has been limited but promising. Doping Mg_2Si and ZnCdO with scandium has been shown to increase the power factor ($\frac{S^2}{\rho}$) significantly [22,23]. Additionally, thin films of ScN are known to have large power factors when compared to other transition metal nitrides [24,25]. Therefore, investigation of other compounds containing scandium is of interest.

Here, we present an investigation of scandium sesquitelluride (Sc_2Te_3). While other rare-earth tellurides have been investigated for high-temperature thermoelectric applications, prior studies of Sc_2Te_3 were limited to structural studies [26,27]. Unlike other $\text{RE}_{3-x}\text{Te}_4$ ($\text{RE} = \text{La}, \text{Ce}, \text{Pr}, \text{Nd}$) compounds, Sc_2Te_3 does not adopt the Th_3P_4 structure type. Men'kov et al. first reported Sc_2Te_3 in the cubic ($Fm\bar{3}m$) structure type, which is a rock salt (NaCl) structure with 1/3 of the Sc sites vacant [26]. White and Dismukes also obtained Sc_2Te_3 in a rhombohedral ($R\bar{3}m$) structure, which can be described as alternating regions of the NaCl and NiAs structure types [27]. Both phases were produced using a similar method of direct reaction of elements, and the reason for the differences in reported crystal structures is still undetermined. However, these structures are relatively complex and would likely be favorable to have intrinsically low-lattice thermal conductivities (κ_L). Furthermore, point-defect scattering from RE vacancies is known to contribute to the low κ_L of the Th_3P_4 structure, where up to 1/9 of the cation positions may be vacant [6,7]. Similarly, the comparatively larger number of cation vacancies in the cubic Sc_2Te_3 structure (1/3 of the Sc positions) may enhance phonon scattering compared to Th_3P_4 compounds.

Although Sc_2Te_3 has traditionally been made using melt synthesis, we employed a low-temperature mechanochemical synthesis to avoid sample inhomogeneity and compositional variations due to the large differences in melting points of Sc and Te (1541 and 449 °C, respectively) [6,7]. After synthesis, the compound was compacted using spark plasma sintering (SPS) and characterized using powder X-ray diffraction (XRD) and scanning electron microscopy (SEM). The high-temperature thermoelectric properties (ρ , S , and κ) were measured up to 1100 K, and zT was calculated.

2. Materials and Methods

2.1. Synthesis

Sc_2Te_3 was synthesized using a mechanochemical approach. Elemental Sc (99.9%, Chemistry Cabinet) and Te shot (99.999%, 5N Plus) were combined in an argon-filled glovebox and placed in a stainless-steel ball mill vial with stainless-steel balls. It was then ball milled (SPEX SamplePrep 8000, SPEX SamplePrep, Metuchen, NJ, USA) for over 10 h until a homogenous, black powder of Sc_2Te_3 was produced. The powder was then compacted in a 12.7-mm graphite die using spark plasma

sintering (SPS) at a temperature above 1450 K and a pressure of 80 MPa for 30 min under vacuum. From geometric measurements, the ingot was found to have a density of 99% the theoretical value (Table S1). A sample was then cut from the ingot using a diamond saw and ground to a thickness of approximately 1 mm for high-temperature measurements.

2.2. Characterization

Powder X-ray diffraction (XRD) data was collected with a Phillips PANalytical X'Pert Pro diffractometer (Philips PANalytical, Westborough, MA, USA) using Cu K α radiation. Due to the Sc₂Te₃ powder being highly air sensitive, the powders were sealed with 1-mm-thick Kapton film on a Si zero background holder under argon. Compacted samples were ground using a mortar and pestle, and scans were performed over a 2θ range of 20°–70°, with a 0.02° step size and a time of 487 s per step. Back-scattered electron (BSE) scanning electron microscope (SEM) images were taken on a Zeiss 1550 VP SEM (Carl Zeiss AG, Oberkochen, Germany).

Once compacted, the sample was stable enough to be handled outside the glovebox; however, a native oxide would form slowly if left out for extended periods (>10 min). Due to this, the sample surface was polished immediately before measurements were taken. A custom-built combined 4-point probe and Hall effect system was used to measure the electrical resistivity and Hall voltage, from which the carrier concentration and Hall mobility were calculated [28]. The Seebeck coefficient was measured using a custom-fabricated instrument [29]. The specific heat capacity was measured using a Netzsch DSC 404 (Netzsch, Selb, Germany), and thermal diffusivity was measured using a Netzsch LFA 457 system (Netzsch, Selb, Germany). The thermal conductivity was calculated by $\kappa = DC_p d$ where κ is the thermal conductivity, D is the thermal diffusivity, C_p is the specific heat capacity, and d is the sample density. The measured C_p is shown in Figure S1.

The temperature-dependent elastic moduli of Sc₂Te₃ was measured by resonant ultrasound spectroscopy (RUS) under flowing Ar using a modified Magflux-RUS Quasar 4000 system (Magflux, Glenview, IL, USA) [30,31]. Buffer-rods were glued to the transducer that extended into the furnace for sample mounting. Cylindrical samples were mounted on a tripod transducer setup, where one transducer induced vibrations and the remaining two detected the specimen resonances. The sinusoidal driving frequency was swept from 0 to 500 kHz. The elastic moduli were measured in 20 K intervals from 303 K up to 673 K. The data was analyzed using commercial Quasar2000 CylModel software (Version 2.68b, Magflux, Glenview, IL, USA) to match the observed and predicted resonant frequencies peaks. At room temperature, 19 peaks were fitted, yielding a standard deviation of 0.09%. Since the elastic tensor value does not change after fitting the first 6 peaks, only the first 6 peaks were used for high-temperature analysis.

High-temperature X-ray diffraction of Sc₂Te₃ was measured from 303 K to 553K in 20 K intervals using a Rigaku Smartlab XRD system (Rigaku, The Woodlands, TX, USA) (Cu K α radiation) equipped with a high-temperature stage. The sample was ground into a fine powder and placed on graphite foil on top of a platinum tray. The measurement was performed under vacuum (10^{−4} Torr) to prevent oxidation. The thermocouple was in contact with the inner part of the platinum tray to increase the accuracy of the temperature measurement. A heating rate of 10 K/min was used with a 1-min hold, and sample height alignments were performed before each measurement to account for the thermal expansion of the holder and sample. Phase purity of the samples was confirmed via peak matching within the ICSD database, and lattice parameters were obtained using peak indexing using PDXL2.

3. Results and Discussion

3.1. Phase Analysis

To verify the phase of the sample, a densified compact was ground using a mortar and pestle and analyzed using powder X-ray diffraction (Figure 1a). The pattern correlated with the cubic ($Fm\bar{3}m$) Sc₂Te₃ structure [26]. A small amount of the rhombohedral phase ($R\bar{3}m$) was detected.

The homogeneity of the sample was further verified by back-scattered electron (BSE) scanning electron microscopy (SEM) (Figure 1b). The uniform contrast reflects the phase homogeneity of the sample. Energy dispersive X-ray spectroscopy (EDS) also confirmed an even distribution of Sc and Te throughout the sample (Figure S1), with dark regions representing residual porosity in the sample. A small number of Fe inclusions were also observed, likely coming from the vials used during ball milling. The measured room temperature lattice parameter value of $a = 5.831 \pm 0.005 \text{ \AA}$ was in excellent agreement with prior literature (5.817 \AA) [26].

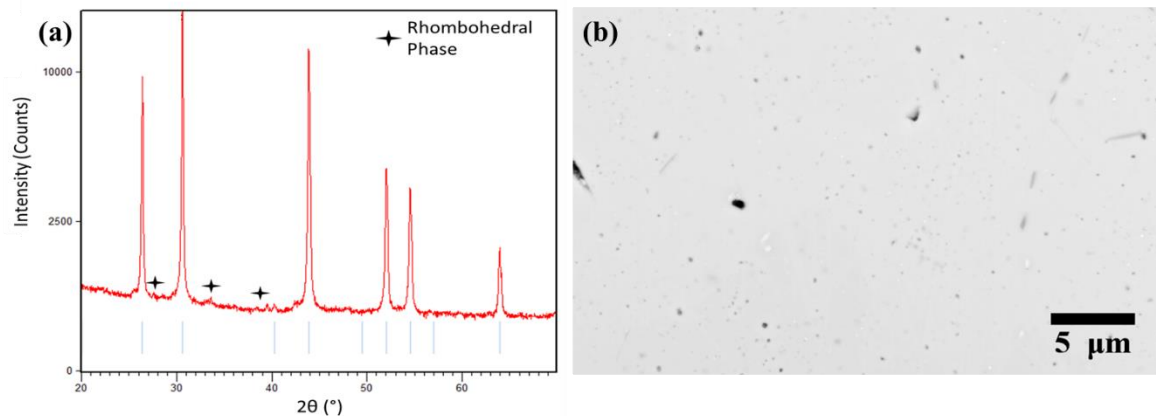


Figure 1. (a) Powder X-ray diffraction pattern of Sc_2Te_3 sample. The pattern agrees well with the Sc_2Te_3 phase (blue lines). A small amount of the rhombohedral Sc_2Te_3 phase was detected and marked. (b) Back-scattered electron (BSE) SEM micrograph of the polished surface of the Sc_2Te_3 . Dark regions are from residual porosity present in the sample. A small number of Fe contaminants (light regions) were observed and confirmed through energy dispersive X-ray spectroscopy (EDS).

3.2. Electronic Transport Properties

The high-temperature electrical resistivity (ρ) of Sc_2Te_3 is shown in Figure 2a. The ρ increases with increasing temperature, as expected for a degenerate semiconductor. The Seebeck coefficient (S) (Figure 2b) was positive, indicating p -type conduction, and was relatively constant from 500–1000 K. The positive S and Hall carrier concentration (Figure 2c) suggest that the sample is slightly Te-rich, relative to the nominal, charge-balanced Sc_2Te_3 composition.

Above 1000 K, a decrease in S and a change in the slope of ρ were observed. Both of these correspond to an increase in the Hall carrier concentration (p_{H}), shown in Figure 2c, indicating minority carrier activation. The Hall mobility (Figure 2d) decreased with increasing temperature, which is expected for acoustic phonon scattering. The decreasing mobility accounts for the increase in resistivity until 900 K, above which the increase in carrier concentration leads to a plateau in ρ . The thermal bandgap (E_g) was calculated to be 0.31 eV using the approximation $S = E_g/2eT_{\text{max}}$, where T_{max} is the temperature where the maximum value of S occurs [32]. This value is lower than the bandgaps for other rare-earth tellurides (approximately 0.9 eV for $\text{La}_{3-x}\text{Te}_4$ and $\text{Pr}_{3-x}\text{Te}_4$) [6,7]. The power factor (S^2/ρ) was calculated by combining S and ρ (Figure 2e). Due to the sharp increase in S at low temperatures, an appreciable power factor is achieved from 400 to 600 K. However, at higher temperatures S^2/ρ decreases from the increased resistivity and reduction in Seebeck.

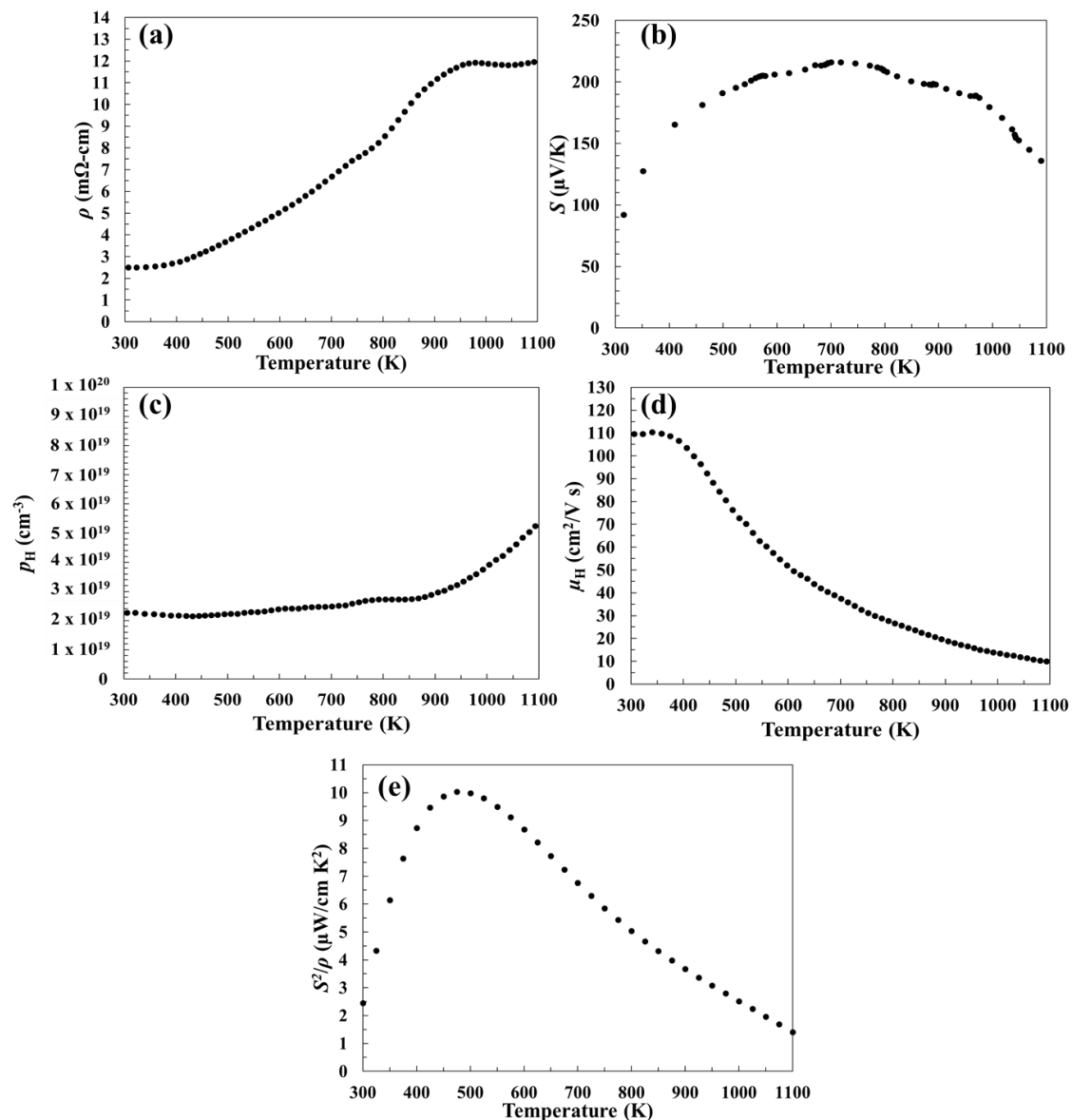


Figure 2. Temperature-dependent (a) electrical resistivity, (b) Seebeck coefficient, (c) Hall carrier concentration, (d) Hall mobility, and (e) power factor of Sc_2Te_3 .

3.3. Thermal Transport Properties

The total thermal conductivity (filled circles in Figure 3a) was found to range from 15 to 22 $\text{mW}\cdot\text{cm}^{-1}\cdot\text{K}^{-1}$, similar to that of other rare-earth tellurides [6,7]. The lattice thermal conductivity (κ_L) was determined by subtracting the electronic contribution (κ_e) from the total thermal conductivity, where κ_e was calculated using the Weidemann–Franz law ($\kappa_e = LT/\rho$). A simplified temperature-dependent Lorenz number (L) was calculated as a function of Seebeck coefficient using the estimation $L = 1.5 + \exp(-|S|/116)$, resulting in values between 1.7 and $2.2 \times 10^{21} \text{ W}\cdot\Omega\cdot\text{K}^{-2}$ [33]. This approximation is calculated from a single parabolic band model and assumes acoustic phonon scattering of charge carriers. κ_L was the primary contributor to the total thermal conductivity (Figure 3a, open circles) with values between 11 and 18 $\text{mW}\cdot\text{cm}^{-1}\cdot\text{K}^{-1}$.

As shown in Figure 4a, the κ_L of Sc_2Te_3 is significantly higher than that of $\text{Pr}_{3-x}\text{Te}_4$ or $\text{La}_{3-x}\text{Te}_4$ [7]. To explain the disparity in κ_L , several factors must be considered. Both structure types contain a large concentration of vacancies on the cation site (30% in Sc_2Te_3 and 11% in the $\text{RE}_{3-x}\text{Te}_4$ samples highlighted here), which leads to significant scattering of high-frequency phonons in all three

cases. We also consider differences in the speed of sound and Grüneisen parameters, evaluated by means of the temperature-dependent elastic moduli and the thermal expansion behavior shown in Figure 4. Resonant ultrasound spectroscopy (RUS) was performed up to 673 K to determine the temperature-dependent Young's (Y) and shear (G) moduli. Although the elastic moduli of Sc_2Te_3 at room temperature are actually softer than those reported for $\text{La}_{3-x}\text{Te}_4$ and $\text{Pr}_{3-x}\text{Te}_4$, the lower theoretical density of Sc_2Te_3 leads to slightly higher longitudinal and transverse speeds of sound (see Table 1) [7]. We also find that Sc_2Te_3 exhibits a lower thermal expansion coefficient and a lower bond softening rate than $\text{RE}_{3-x}\text{Te}_4$ ($\text{RE} = \text{Pr}$ or La) samples (see Figure 4b–d). This is indicative of a lower Grüneisen parameter in Sc_2Te_3 , possibly due to the smaller coordination numbers of the cation site (6-fold for Sc versus 8-fold for La and Pr) [34,35]. Indeed, estimating the average thermodynamic Grüneisen parameter as $\gamma = \alpha B / C_v \rho$ (α is the volume thermal expansion coefficient, B is the bulk modulus, C_v is the heat capacity, and ρ is the theoretical density) yields much lower values for Sc_2Te_3 , which would lead to lower rates of phonon–phonon scattering. Thus, the combination of a slightly higher sound velocity and lower Grüneisen parameter in Sc_2Te_3 is likely the origin of its higher κ_L in the measured temperature range.

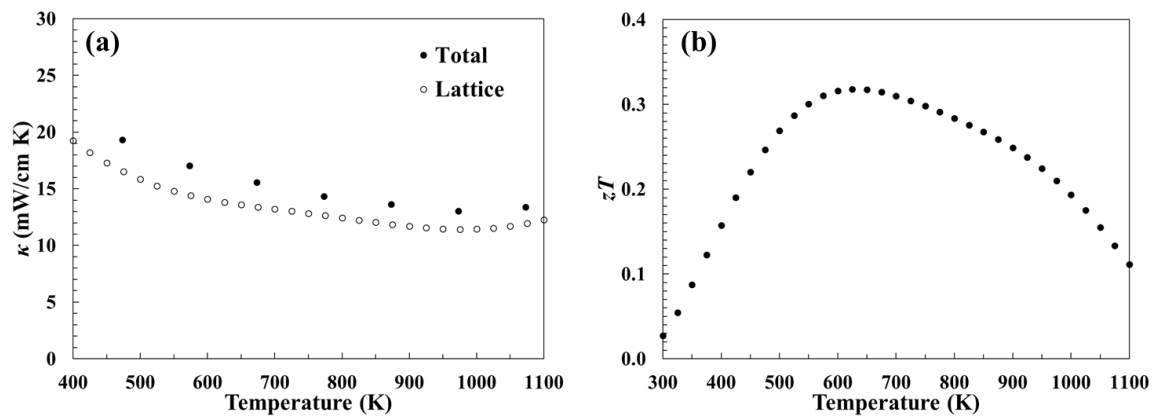


Figure 3. Temperature-dependent (a) thermal conductivity and (b) thermoelectric figure of merit.

Table 1. Elastic moduli, speed of sound, density, volumetric coefficient of thermal expansion, and Grüneisen parameters for Sc_2Te_3 compared with $\text{PrTe}_{1.46}$ and $\text{LaTe}_{1.46}$ [7].

Parameters	$\text{PrTe}_{1.46}$	$\text{LaTe}_{1.46}$	Sc_2Te_3
Young's modulus, Y (GPa)	68.6	70.1	65.4
Shear modulus, G (GPa)	27.1	27.6	26.7
Bulk modulus, B (GPa)	49.3	50.9	39.6
Long velocity, v_L (m/s)	3543	3642	3773
Transverse velocity, v_T (m/s)	1994	2042	2247
Density, ρ (g/cm^3)	6.804	6.607	5.285
Volume CTE ($10^{-5}/\text{K}$)	5.06	4.62	3.60
Grüneisen parameter, γ	1.96	1.89	1.03

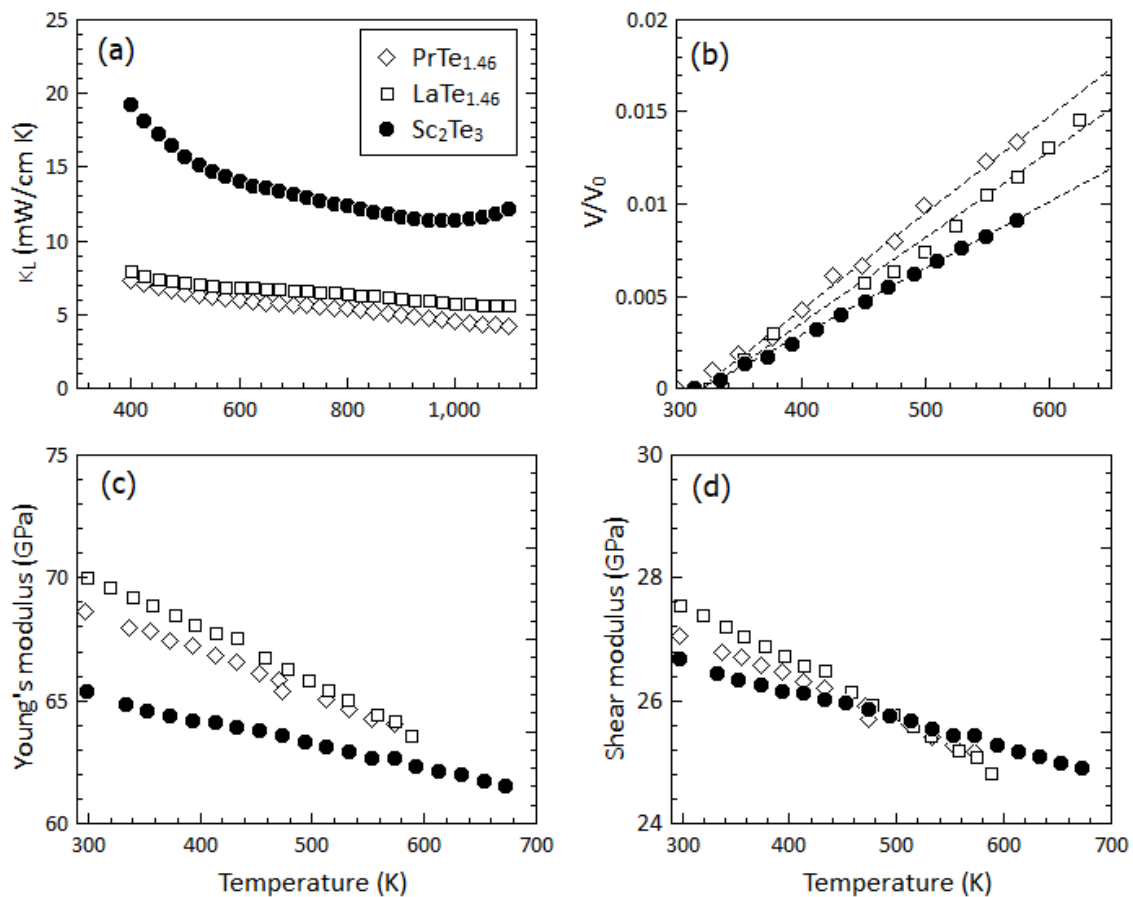


Figure 4. A comparison of (a) the lattice thermal conductivity, (b) experimental volume thermal expansion, V/V_0 (c) the temperature-dependent Young's moduli, and (d) shear moduli of PrTe_{1.46}, LaTe_{1.46}, and Sc₂Te₃. Data for PrTe_{1.33} and LaTe_{1.46} are from reference [7].

3.4. Dimensionless Thermoelectric Figure of Merit

The thermal and electronic transport properties were used to calculate the dimensionless thermoelectric figure of merit (zT) (Figure 3b). The sharp rise in the power factor at low temperatures allows for Sc₂Te₃ to attain a maximum zT value of 0.3 from 500 to 750 K. Additionally, the relative flatness of the Seebeck coefficient with respect to temperature causes zT to maintain values close 0.3 over the mid-temperature range. This peak thermoelectric performance at intermediate temperatures contrasts the behavior of other rare-earth tellurides, where their properties optimize in the high-temperature regime (>1200 K) [2,6,7].

4. Conclusions

Sc₂Te₃ was successfully synthesized using a mechanochemical approach and compacted using spark plasma sintering. Powder XRD confirmed the samples were Sc₂Te₃ with the space group $Fm\bar{3}m$. The temperature-dependent electronic and thermal transport properties were measured. The power factor was found to achieve values near 10 $\mu\text{W}/\text{m}\cdot\text{K}^2$ in the intermediate-temperature range due to a large, p -type Seebeck coefficient. κ_L was determined to be the dominant contribution to the thermal conductivity. Compared with RE_{3-x}Te₄ (RE = Pr or La) compounds, the κ_L of Sc₂Te₃ was higher due to its higher speed of sound and lower Grüneisen parameter. A zT value of 0.3 was achieved in the mid-temperature range of 500–750 K. Modification to the carrier concentration or addition of dopants for point-defect scattering may help improve the properties of Sc₂Te₃.

Supplementary Materials: The following are available online at <http://www.mdpi.com/1996-1944/12/5/734/s1>. Figure S1. Temperature-dependent heat capacity. Table S1. Sample density measurements.

Author Contributions: Conceptualization, D.C. and S.K.B.; methodology, D.C. and S.K.B.; validation, D.C. and S.K.B.; formal Analysis, D.C., K.L., W.P., A.Z., and S.K.B.; investigation, D.C., K.L., and W.P.; resources, D.C., W.P., A.Z., and S.K.B.; data curation, D.C., K.L., and W.P.; writing—original draft preparation, D.C.; writing—review and editing, D.C., K.L., W.P., A.Z., J.-P.F., and S.K.B.; visualization, D.C.; supervision, S.K.B. and J.-P.F.; project administration, S.K.B.; and funding acquisition, S.K.B. and J.-P.F.

Funding: This work was performed at the California Institute of Technology/Jet Propulsion Laboratory under contract with the National Aeronautics and Space Administration. This work was supported by the NASA Science Missions Directorate under the Radioisotope Power Systems Program’s Fundamental Research Task. A.Z. acknowledges funding from the National Science Foundation (NSF) under Award # DMR SSMC-1709158.

Acknowledgments: The authors would like to thank Ryan H. DeBlock for his aid with the source scandium used in this study.

Conflicts of Interest: The authors declare no conflict of interest.

References

1. Fleurial, J.-P. Thermoelectric power generation materials: Technology and application opportunities. *JOM* **2009**, *61*, 74–85. [[CrossRef](#)]
2. Wood, C. Materials for thermoelectric energy conversion. *Rep. Prog. Phys.* **1988**, *51*, 459–539. [[CrossRef](#)]
3. Yang, J.; Caillat, T. Thermoelectric materials for space and automotive power generation. *MRS Bull.* **2006**, *31*, 224–229. [[CrossRef](#)]
4. Vining, C.B.; Fleurial, J.-P. *Silicon-Germanium: An Overview of Recent Development*; AIP Press: Albuquerque, NM, USA, 1993; pp. 87–120.
5. Snyder, G.J.; Toberer, E.S. Complex Thermoelectric Materials. *Nat. Mater.* **2008**, *7*, 105–114. [[CrossRef](#)] [[PubMed](#)]
6. May, A.F.; Fleurial, J.-P.; Snyder, G.J. Thermoelectric performance of lanthanum telluride produced via mechanical alloying. *Phys. Rev. B* **2008**, *78*, 125205. [[CrossRef](#)]
7. Cheikh, D.; Hogan, B.E.; Vo, T.; von Allmen, P.; Lee, K.; Smiadak, D.M.; Zevalkink, A.; Dunn, B.S.; Fleurial, J.-P.; Bux, S.K. Praseodymium Telluride: A High Temperature, High ZT Thermoelectric Material. *Joule* **2018**, *2*, 698–709. [[CrossRef](#)]
8. Vickery, R.C.; Muir, H.M. Thermoelectric properties of rare earth chalcogenides. *Adv. Energy Convers.* **1961**, *1*, 179–186. [[CrossRef](#)]
9. Ma, J.M.; Clarke, S.M.; Zeier, W.G.; Vo, T.; von Allmen, P.; Snyder, G.J.; Kaner, R.B.; Fleurial, J.-P.; Bux, S.K. Mechanochemical synthesis and high temperature thermoelectric properties of calcium-doped lanthanum telluride $\text{La}_{3-x}\text{Ca}_x\text{Te}_4$. *J. Mater. Chem. C* **2015**, *3*, 10459–10466. [[CrossRef](#)]
10. Taher, S.M.; Gruber, J.B. Thermoelectric efficiency of rare earth sesquisulfides. *Mat. Res. Bull.* **2001**, *16*, 1407–1412. [[CrossRef](#)]
11. Cutler, M.; Leavy, J.F.; Fitzpatrick, R.L. Electronic Transport in Semimetallic Cerium Sulfide. *Phys. Rev* **1964**, *133*, A1143. [[CrossRef](#)]
12. May, A.F.; Singh, D.J.; Snyder, G.J. Influence of band structure on the large thermoelectric performance of lanthanum telluride. *Phys. Rev. B* **2009**, *9*, 153101. [[CrossRef](#)]
13. Vo, T.; von Allmen, P.; Huang, C.-H.; Ma, J.M.; Bux, S.K.; Fleurial, J.-P. Electronic and thermoelectric properties of Ce_3Te_4 and La_3Te_4 computed with density functional theory with on-site Coulomb interaction correction. *Appl. Phys.* **2014**, *116*, 133701. [[CrossRef](#)]
14. Connelly, N.G.; Damhus, T.; Hartshorn, R.M.; Hutton, A.T. Elements in the Periodic Table. In *Nomenclature of Inorganic Chemistry*, 1st ed.; The Royal Society of Chemistry: Cambridge, UK, 2005; ISBN 0-85404-438-8.
15. Ahmad, Z. The Properties and Application of Scandium-Reinforced Aluminum. *JOM* **2003**, *55*, 35–39. [[CrossRef](#)]
16. Parker, B.A.; Zhou, Z.F.; Nolle, S.P. The Effect of Small Addition of Scandium on the Properties of the Aluminum Alloys. *J. Mater. Sci.* **1995**, *30*, 452–458. [[CrossRef](#)]
17. Sawtell, R.R.; Jensen, C.L. Mechanical Properties and Microstructure of Al-Mg-Sc Alloys. *Metal. Trans. A* **1990**, *21*, 421–430. [[CrossRef](#)]

18. Jindal, V.; De, P.K.; Venkateswarlu, K. Effect of Al₃Sc precipitates on the work hardening behavior of aluminum–scandium alloys. *Mater. Lett.* **2006**, *60*, 3373–3375. [[CrossRef](#)]
19. Wygant, B.R.; Jarvis, K.A.; Chemelewski, W.D.; Mabayoje, O.; Celio, H.; Mullins, C.B. Structural and Catalytic Effects of Iron- and Scandium-Doping on a Strontium Cobalt Oxide Electrocatalyst for Water Oxidation. *ACS Catal.* **2016**, *6*, 1122–1133. [[CrossRef](#)]
20. Yin, Y.M.; Xiong, M.W.; Yang, N.T.; Tong, Z.; Guo, Y.Q.; Ma, Z.F.; Sun, E.; Yamanis, J.; Jing, B.Y. Investigation on thermal, electrical, and electrochemical properties of scandium-doped Pr_{0.6}Sr_{0.4}(Co_{0.2}Fe_{0.8})_(1-x)Sc_xO_{3-d} as cathode for IT-SOFC. *Int. J. Hydrogen Energy* **2011**, *36*, 3989–3996. [[CrossRef](#)]
21. Zeng, P.; Ran, R.; Shao, Z.; Yu, H.; Liu, S. Effects of Scandium Doping Concentration on The Properties of Strontium Cobalt Oxide Membranes. *Braz. J. Chem. Eng.* **2009**, *26*, 563–574. [[CrossRef](#)]
22. Han, L.; Christensen, D.V.; Bhowmik, B.; Simonsen, S.B.; Hung, L.T.; Abdellahi, E.; Chen, Y.Z.; Nong, N.V.; Linderoth, S.; Pryds, N. Scandium-doped zinc cadmium oxide as a new stable n-type oxide thermoelectric material. *J. Mater. Chem. A* **2016**, *4*, 12221–12231. [[CrossRef](#)]
23. Menga, Q.S.; Fana, W.H.; Chena, R.X.; Munirb, Z.A. Thermoelectric properties of Sc- and Y-doped Mg₂Si prepared by field-activated and pressure-assisted reactive sintering. *J. Alloys Compd.* **2011**, *509*, 7922–7926. [[CrossRef](#)]
24. Saha, B.; Garbrecht, M.; Perez-Taborda, J.A.; Fawey, M.A.; Koh, Y.R.; Shakouri, A.; Martin-Gonzalez, M.; Hultman, L.; Sands, T.D. Compensation of native donor doping in ScN: Carrier concentration control and p-type ScN. *Appl. Phys. Lett.* **2017**, *110*, 252104. [[CrossRef](#)]
25. Kerdsonpanya, S.; Van Nong, N.; Pryds, N.; Žukauskaitė, A.; Jensen, J.; Birch, J.; Lu, J.; Hultman, L.; Wingqvist, G.; Eklund, P. Anomalous high thermoelectric power factor in epitaxial ScN thin films. *Appl. Phys. Lett.* **2011**, *99*, 232113. [[CrossRef](#)]
26. Men'kov, A.A.; Komissarova, L.N.; Simanov, Y.P.; Spitsyn, V.I. On Scandium Chalkogenides. *Dokl. Akad. Nauk SSSR* **1961**, *141*, 364–367.
27. White, J.G.; Dismukes, J.P. The Crystal Structure of Scandium Sesquitelluride. *Inorg. Chem.* **1965**, *4*, 1760–1763. [[CrossRef](#)]
28. Borup, K.A.; Toberer, E.S.; Zoltan, L.D.; Nakatsukasa, G.; Errico, M.; Fleurial, J.-P.; Iversen, B.B.; Snyder, G.J. Measurement of the electrical resistivity and Hall coefficient at high temperatures. *Rev. Sci. Instrum.* **2012**, *83*, 123902. [[CrossRef](#)] [[PubMed](#)]
29. Wood, C.; Zoltan, D.; Stapfer, G. Measurement of Seebeck coefficient using a light pulse. *Rev. Sci. Instrum.* **1985**, *56*, 719–722. [[CrossRef](#)]
30. Li, G.; Gladden, J.R. High temperature resonant ultrasound spectroscopy: A review. *Int. J. Spectrosc.* **2010**, *2010*. [[CrossRef](#)]
31. ASTM C1548-02. *Standard Test Method for Dynamic Young's Modulus, Shear Modulus, and Poisson's Ratio by Impulse Excitation of Vibration*; ASTM International: West Conshohocken, PA, USA, 2002.
32. Goldsmid, H.J.; Sharp, J.W. Estimation of the thermal band gap of a semiconductor from seebeck measurements. *J. Electron. Mater.* **1999**, *28*, 869–872. [[CrossRef](#)]
33. Kim, H.S.; Gibbs, Z.M.; Tang, Y.; Wang, H.; Snyder, G.J. Characterization of Lorenz number with Seebeck coefficient measurement. *APL Mater.* **2015**, *3*, 041506. [[CrossRef](#)]
34. Zeier, W.; Zevalkink, A.; Gibbs, Z.M.; Hautier, G.; Kanatzidis, M.G.; Snyder, G.J. Thinking like a chemist: Intuition in thermoelectric materials. *Angew. Chem. Int. Ed.* **2016**, *55*, 6826–6841. [[CrossRef](#)] [[PubMed](#)]
35. Miller, S.A.; Gorai, P.; Ortiz, B.R.; Goyal, A.; Gao, D.; Barnett, S.A.; Mason, T.O.; Snyder, G.J.; Lv, Q.; Stevanović, V.; et al. Capturing Anharmonicity in a Lattice Thermal Conductivity Model for High-Throughput Predictions. *Chem. Mater.* **2017**, *29*, 2494–2501. [[CrossRef](#)]

